Deep Eastern Boundary Currents: Realistic Simulations and Vorticity Budgets

XIAOTING YANG,[a] ELI TZIPERMAN,[a,b] AND KEVIN SPEER[c,d]

[a] *Department of Earth and Planetary Sciences, Harvard University, Cambridge, Massachusetts;* [b] *School of Engineering and Applied Sciences, Harvard University, Cambridge, Massachusetts;* [c] *Geophysical Fluid Dynamics Institute, Florida State University, Tallahassee, Florida;* [d] *Department of Earth, Ocean, and Atmosphere Sciences, Florida State University, Tallahassee, Florida*

(Manuscript received 21 January 2020, in final form 14 August 2020)

ABSTRACT: Concentrated poleward flows near the eastern boundaries between 2- and 4-km depth have been observed repeatedly, particularly in the Southern Hemisphere. These deep eastern boundary currents (DEBCs) play an important role in setting the large-scale tracer distribution and have nonnegligible contribution to global transports of mass, heat, and tracers, but their dynamics are not well understood. In this paper, we first demonstrate the significant role of DEBCs in the southeastern Atlantic, Indian, and Pacific Oceans, using the Southern Ocean State Estimate (SOSE) data assimilating product, and using high-resolution regional general circulation model configurations. The vorticity balances of these DEBCs reveal that, over most of the width of such currents, they are in an interior-like vorticity budget, with the meridional advection of planetary vorticity βv and vortex stretching fw_z being the largest two terms, and with contributions of nonlinearity and friction that are of smaller spatial scale. The stretching is shown, using a temperature budget, to be largely forced by resolved or parameterized eddy temperature transport. Strongly decaying signals from the eastern boundary in friction and stretching form the dominant balance in a sublayer close to the eastern boundary. The temporal variability of DEBCs is then examined, to help to interpret observations that tend to be sporadic in both time and space. The probability distribution functions of northward velocity in DEBC regions are broad, implying that flow reversals are common. Although the regions of the simulated DEBCs are generally local minima of eddy kinetic energy, they are still constantly releasing westward-propagating Rossby waves.

KEYWORDS: Ocean; Boundary currents; Ocean circulation; Ocean dynamics

1. Introduction

Intense currents along the western boundaries, for example, the Gulf Stream and underlying deep western boundary current in the North Atlantic Ocean, and similar western boundary currents in other basins, are striking features of the global ocean circulation. The ocean interior flow is, in contrast, typically dominated by an energetic eddy field, from which the large-scale gyres emerge in a time average. The basic dynamics of the western boundary currents have been explained by the linear theories of Stommel and Munk (Stommel 1948; Munk 1950), and their role in the deep circulation by Stommel and Arons (1960), although it is now understood that nonlinearity and bottom torque are important as well (e.g., Hughes and De Cuevas 2001). However, concentrated flows have also been observed near the eastern boundaries. Coastally trapped eastern boundary currents are found concentrated at shallow levels, driven by wind or surface buoyancy gradients (Hickey 1979; Thompson 1984). More relevant to this work, deep eastern boundary currents (DEBCs) have been consistently observed at depths between 2 and 4 km, with significant transports (Sloyan and Rintoul 2001) and also found in numerical simulations (Tamsitt et al. 2017). These DEBCs also play an important yet underappreciated role in the climate system, with dynamics that are unclear, and are the focus of this paper and a companion study (X. Yang et al. 2020, unpublished manuscript).

The existence of a DEBC in the southeastern Pacific Ocean, between 2- and 4-km depth, has been repeatedly revealed by tracer distributions typical of northern sources, including low oxygen, high nutrients, and low large-scale potential vorticity, indicating a southward flow of the weakly stratified Pacific Deep Water along the eastern boundary (Warren 1973; Tsimplis et al. 1998; Wijffels et al. 2001; Well et al. 2003; Faure and Speer 2012; Chretien and Speer 2019). Specifically, the signature of high concentration of δ^3He in this flow implies that it is partially fed by zonal flows from the west, where the East Pacific Rise is a major source of ^{3}He (Well et al. 2003). This supply from the west turns out to be an important part of the dynamics, as we will see below. Significant southward transports near the South Pacific eastern boundary are indeed derived from geostrophic calculations, inverse box models and water mass analysis (Wunsch et al. 1983; Tsimplis et al. 1998; Wijffels et al. 2001; Sloyan and Rintoul 2001; Well et al. 2003; Faure and Speer 2012), ranging from 2 to 10 Sv ($1\,\text{Sv} \equiv 10^6\,\text{m}^3\,\text{s}^{-1}$). Although some of these analyses are prone to biases due to instantaneous features such as passing eddies, observations of persistent large-scale tracer patterns, direct velocity measurements and transport analysis at different latitudes (Chretien and Speer 2019) indicate that the DEBC is robust. Long-term direct velocity measurements show a southward flow near the eastern boundary, above the prominent Peru–Chile trench and also to the west of the trench (Shaffer et al. 1995, 2004), with core speeds evaluated between

Supplemental information related to this paper is available at the Journals Online website: https://doi.org/10.1175/JPO-D-20-0002.s1.

Corresponding author: Xiaoting Yang, xiaoting_yang@g.harvard.edu

DOI: 10.1175/JPO-D-20-0002.1

1 and 30 cm s^{-1}. These southward currents show temporal variability (Shaffer et al. 1995, 2004; Chretien and Speer 2019), but their total eddy kinetic energy is found to be low (Shaffer et al. 1995).

In the southeastern Atlantic Ocean, salinity and oxygen are found to form deep high concentration cores near the eastern boundary that decay southward along the boundary (Warren and Speer 1991; Arhan et al. 2003), consistent with a southward flow of deep water with North Atlantic Deep Water (NADW) characteristics. An eastward zonal flow of NADW feeding the South Atlantic DEBC was found by Speer et al. (1995) and supported by observations with neutrally buoyant floats (Hogg and Thurnherr 2005). An inverse box model constrained by the velocities of these floats estimates the southward transport near the eastern boundary to be 3.2 Sv at 18°S and 5.0 Sv at 30°S in the NADW layer, comparable to estimates by Arhan et al. (2003) of 2.7 Sv near 20°S and 7.5 Sv near 30°S, and estimates of about 4 Sv at 37°S by Sloyan and Rintoul (2001).

Similarly, in the southeastern Indian Ocean, water masses of northern origin, with weaker stratification, lower oxygen, and higher nutrients, are also found near the eastern boundaries at the same depth range, in the Perth Basin and South Australia Basin (Toole and Warren 1993; Tamsitt et al. 2019), again consistent with a southward eastern boundary flow. An inverse box model constrained by these hydrographic data, including a silicate budget, indicates southward transport near the eastern boundary as large as 6 Sv in the NADW layer (Robbins and Toole 1997). In an inverse study of ocean transport (Sloyan and Rintoul 2001), the concentrated DEBC southward transport of Lower Circumpolar Deep Water is constrained to 5 Sv and that of Indian Deep Water (IDW) and Upper Circumpolar Deep Water (UCDW) is about 7 Sv. In the same study, there is also a southward concentrated transport west of the Naturaliste Plateau of about 5 Sv, also found in the IDW/UCDW layer. This branch of southward flow has been directly observed (Sloyan 2006) with a core speed of about 10 cm s^{-1} at 3.2-km depth.

Although these deep eastern boundary currents are important branches of the global meridional overturning circulation (Wunsch et al. 1983; Sloyan and Rintoul 2001; Arhan et al. 2003), state-of-the-art climate models and data assimilating products without sufficiently high horizontal resolution do not simulate them at the right position or with the right magnitude. Some data assimilating products give a more satisfactory representation of the DEBCs [e.g., the Southern Ocean State Estimate (SOSE); Mazloff et al. 2010], although this may be because the model is initialized from observations and is integrated for a relatively short time.

Recently, Yang et al. (2020) suggested that the DEBCs are mostly driven by interior-like vorticity dynamics with the advection of planetary vorticity balanced by stretching ($\beta v = f w_z$), and with a frictional layer only at the eastern edge of the DEBCs. We further elaborate on this work here, and divide our analysis of the deep eastern boundary currents into two parts: this paper, using realistic models, and a companion study (X. Yang et al. 2020, unpublished manuscript) with idealized simulations and theoretical analysis. In this paper we first evaluate the contribution of DEBCs to mass and tracer transports using realistic simulations and the Biogeochemical Southern Ocean State Estimate (B-SOSE, iteration 122, from 1 January 2008 to 21 December 2012; Verdy and Mazloff 2017). We show that, while they may seem weak and sometimes have nearby compensating equatorward recirculation, the currents nevertheless have a significant effect on the deep tracer distributions and therefore are a fundamental element of the deep circulation. The companion study (X. Yang et al. 2020, unpublished manuscript), examines the dynamics of these DEBCs using idealized GCM configurations and a simple vorticity model, allowing us to develop a more detailed understanding of the dynamics of DEBCs and their dependence on topographic structure at the eastern boundary.

Shallower concentrated flows near eastern boundaries have also been observed, of course (Hickey 1979; Thompson 1984; Peliz et al. 2003), and many ideas suggested for their dynamics, as reviewed in the companion study (X. Yang et al. 2020, unpublished manuscript). There, we show, however, that DEBCs exist as a result of very different dynamics than those suggested for their shallow counterparts, involving an ocean-interior vorticity balance over most of the width of the current, with special, boundary-current-like dynamics only very close to the eastern boundary.

The general properties of the DEBCs discussed here are that these currents carry northern-origin water masses southward. The vorticity dynamics of these currents is consistent with planetary geostrophy (usually associated with large-scale flow in the interior of ocean basins) offshore, and is strongly modified by friction close to the eastern edge. The vortex stretching term in the planetary vorticity balance maintaining these currents is sensitive to bathymetry. This paper is organized as follows. In section 2 we will discuss the tracer distribution, velocity, and estimated transport of the DEBCs in multiple basins, based on SOSE because of its focus on the Southern Hemisphere. The purpose is to demonstrate that while DEBCs seem transient, weak, and at times with nearby compensating recirculation, their effect on the large-scale tracer distributions and dynamics is significant. In section 3 we analyze the DEBCs simulated in regional GCM configurations, and in particular their vorticity budget. The vorticity budget will be further elucidated in the companion study (X. Yang et al. 2020, unpublished manuscript) to identify the dynamics of DEBCs. In section 4 we analyze the temporal variability of the DEBCs in SOSE and our regional models with an eye toward the interpretation of "snapshot" observations of these complex, time-dependent flows. The roles of resolved or parameterized eddies in the temperature, momentum and vorticity budgets were also examined throughout this paper and the eddies were found to play different roles in these budgets. We conclude in section 5.

2. Deep eastern boundary currents in SOSE

The distribution of tracers in ocean basins is a good indicator of average ocean circulation and currents, but it is difficult to estimate the horizontal distributions of time-averaged tracer fields in the global ocean in a dynamically self-consistent way because observations are usually spatially and temporally sparse. In this section we therefore use B-SOSE to demonstrate that tracer distributions show similarity with observations and indicate the persistent existence and significant effects of poleward DEBCs.

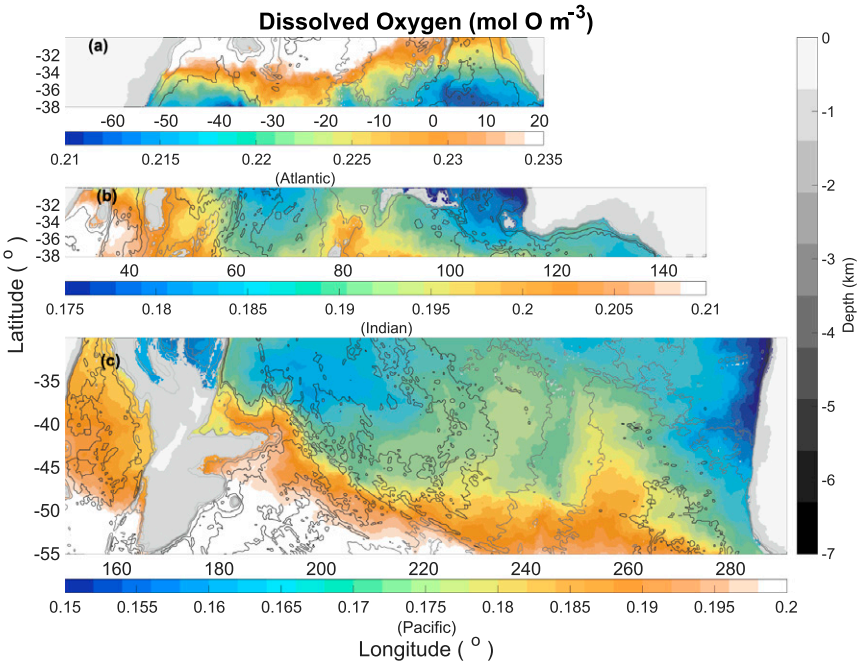

FIG. 1. Dissolved oxygen at a depth of 2610 m (colors) for the (a) South Atlantic Ocean, (b) south Indian Ocean, and (c) South Pacific Ocean. Dark-gray patch: the location of solid earth at the depth of 2610 m; light-gray patch: the location of the continents at the sea surface; gray-scale contours: bathymetry (the gray-scale color bar is only for the bathymetry contours and is not related to the patches). Note that different color ranges are used for different ocean basins.

a. Tracer distributions along eastern boundaries in B-SOSE

We analyzed the distribution of dissolved inorganic carbon (DIC), nitrate, oxygen, phosphate, salinity, and large-scale potential vorticity ($f\partial_z\sigma$) in B-SOSE, for the South Atlantic Ocean (69°W–21°E, 55°–30°S), south Indian Ocean (27.9°–147.9°E, 38.1°–30°S), and South Pacific Ocean (149.9°–290.9°E, 55°–30°S). The South Australia Basin is included in the analysis for the south Indian Ocean because there is an important outflow into the Southern Ocean along the eastern boundary of this basin (Tamsitt et al. 2019). The horizontal resolution of the data assimilating product is 1/6°, and there are 52 vertical layers whose thickness ranges from 4.6 m near the surface to 400 m near the bottom.

At a depth of 2.5 km, the northern part of the South Atlantic Ocean is occupied by a water mass that is low in DIC, nitrate, and phosphate and high in oxygen and salinity, while the water mass in the southern part of the South Atlantic Ocean is characterized by an opposite signal of these tracers (Fig. 1a and Figs. 1–4 in the online supplemental material). This implies that a body of NADW higher in salinity and of more recent ventilation history flows into the South Atlantic Ocean from the north. The tracers form tongue-like structures not only along the western boundary but also on the eastern boundary, consistent with observations (Arhan et al. 2003; Warren and Speer 1991), indicating southward deep flows near the eastern boundaries. Along the western coast of Africa, signals of weak stratification and low potential vorticity are also found (Fig. 2a).

In the south Indian and South Pacific Oceans, the same tracers indicate that water masses of a southern origin, characterized by low nutrient/DIC and high oxygen, flow northward mainly against the western boundaries of these ocean basins (Fig. 1b for the south Indian Ocean, Fig. 1c for South Pacific Ocean, and Figs. 1–4 of the online material). In the South Pacific Ocean, two oxygen minima intrusions are seen in B-SOSE: a weaker one exists between 35° and 40°S, east of the Tonga-Kermadec Ridge, and a stronger oxygen minimum is observed from 30°S to near the southern end of the South American continent. This structure of a double oxygen minimum is consistent with observations (Warren 1973; Wijffels et al. 2001). Unlike the South Atlantic Ocean, the northern part of the South Pacific and Indian Oceans are occupied by older water masses than their southern parts, that are high in nutrients and DIC, and low in oxygen and salinity (Figs. 1b,c and online supplemental Figs. 1–4). The tongue-like structures in these tracers along the eastern boundaries of each ocean are also clear, and are consistent with a southward current in these areas, carrying old, weakly stratified Indian Deep Water or Pacific Deep Water poleward (Toole and Warren 1993; Wijffels et al. 2001; Faure and Speer 2012; Tamsitt et al. 2019). Low potential vorticity is observed in the south Indian and South Pacific Oceans near the eastern boundaries (Figs. 2b,c). Note that the low potential vorticity in the South Pacific Ocean along and above the East Pacific Rise is related to the fact that isotherms dip down toward the ridge crest (Warren 1973) and is far from the DEBCs of interest here.

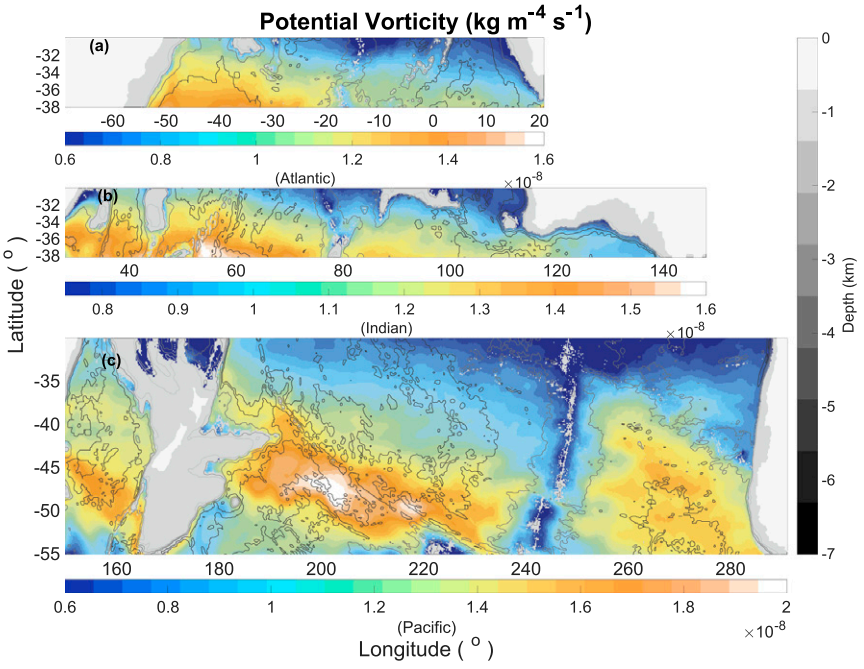

FIG. 2. As in Fig. 1, but for potential vorticity $f\sigma_z$.

Given the (at least qualitative) agreement of the tracer distributions in B-SOSE with observations, we conclude the B-SOSE product is consistent with the presence of significant eastern and western boundary currents. The tongue-like tracer distributions near the eastern boundary, with characteristics of water farther north, indicate the persistent presence of poleward flows concentrated near the eastern boundaries of the southeastern Atlantic, Indian, and Pacific Oceans. We examine these simulated currents in the next section.

b. *Deep eastern boundary current velocities and transports in B-SOSE*

Concentrated poleward flows below 1-km depth are simulated in the South Atlantic, south Indian, and South Pacific Oceans in B-SOSE near the eastern boundaries (Fig. 3), consistent with the tracer patterns discussed in the previous section. In the southeastern Atlantic Ocean, a core of concentrated southward flow against the eastern boundary exists between 1- and 4-km depth, with the velocity maximum exceeding 5 cm s^{-1}. Such a poleward flow in the southeastern Atlantic has also been observed using moored current meters and ADCPs (Nelson 1989; Clement and Gordon 1995). Figure 3a shows that this DEBC starts at 35°S, is fed there by a semizonal flow from the west and extends to the southern tip of the African continent. In the southeastern Indian Ocean, similar DEBCs are also observed between 1- and 5-km depth (at 37°S) but with a weaker magnitude (Fig. 3b). These concentrated Indian Ocean southward flows are found between 35° and 40°S along the western coast of Australia, between 40° and 45°S east of the Naturaliste Plateau and starting at 48°S to near the southern boundary of the Australian continent. The latter component is potentially important because it may be an outflow linking the south Indian Ocean and the Southern Ocean (Tamsitt et al. 2019), hence we will focus on this component in the following.

Figure 3c shows concentrated southward flows in two latitudinal bands in the southeastern Pacific Ocean, one between 35° and 40°S and another one starting at 45°S, extending to the south and connecting to an important outflow to Drake Passage and the Southern Ocean (Well et al. 2003). The DEBC at higher latitudes shows alternating meridional velocity in time and the southward flow only emerges in the time-averaged picture, while the southward flow at lower latitudes exists during most of the year and only shows variability in magnitude. The high-latitude South Pacific DEBC experiences the regular influence of eddies whose magnitude are at least comparable to the mean flow, similar to the DEBCs in the Atlantic and Indian Oceans. Here, we focus on the branch at lower latitudes, because it has a more coherent structure and because it may be in a different dynamical regime than those in the Indian and Atlantic Oceans. Figure 3f shows that the Pacific DEBC at lower latitudes is on the eastern flank of the Peru–Chile trench and coexists with a strong northward flow immediately to its west. While the net transport of these coexisting flows may not be large, the tracer distributions, including large-scale potential vorticity, examined above clearly show the important net effect of the DEBC on the large-scale dynamics and transports. The magnitude of the southeastern Pacific DEBC in B-SOSE is weaker compared to the observed DEBC in repeated instantaneous hydrographic sections at 32.5°S (Chretien and Speer 2019), however, the time-dependent nature of these flows (section 4) makes it difficult to assess the model–data differences.

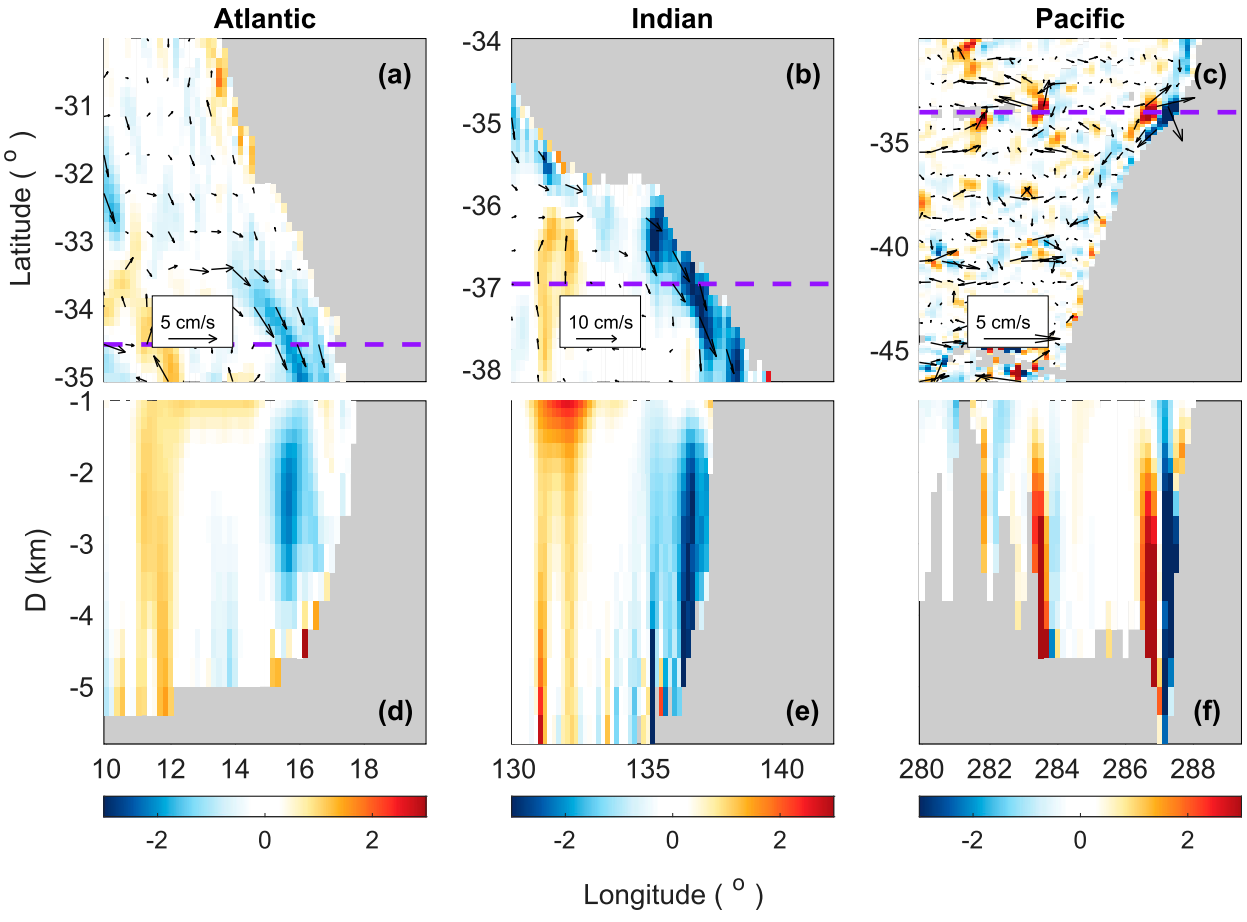

FIG. 3. Meridional velocity (SOSE), with horizontal maps of northward velocity (color) and velocity vectors (black arrows) at the depth of the DEBC cores for the (a) southeastern Atlantic Ocean (3-km depth), (b) southeastern Indian Ocean (2.6-km depth), and (c) southeastern Pacific Ocean (2.8-km depth) and vertical sections of meridional velocity (color) for the (d) southeastern Atlantic Ocean (36.8°S), (e) southeastern Indian Ocean (37.0°S), and (f) southeastern Pacific Ocean (33.5°S). The dashed purple lines in (a)–(c) indicate the latitude at which the vertical sections are taken. Note that different color ranges are used for different ocean basins.

To be able to compare the strengths of DEBCs to other deep currents, cumulative transports (integrated westward from the eastern boundary) between 2.5 and 3.5 km in each ocean are calculated (Fig. 4). Concentrated transports are observed near the eastern boundaries of all three basins. Within three degrees from the eastern boundary, the cumulative southward transports in each basin are 4.4 (Atlantic), 4.5 (Indian), and 0.3 (Pacific) Sv. In the South Atlantic Ocean, west of longitude 40°W, there is northward transport of about 1.5 Sv in the first 2° of longitude and southward transport of about 5 Sv farther east. The net transport near the western boundary is thus about 3.5 Sv southward, comparable to the 4.5 Sv transport near the eastern boundary. The Indian Ocean cumulative transport is calculated along 37°S, where there is no landmass on the west, and therefore there is no western boundary current signal in Fig. 4c. In the South Pacific Ocean, the strong transport east of the Tonga Ridge is about 6 Sv with a 3 Sv cancellation that is due to recirculation to the east. The contribution from the eastern boundary in this case is limited to only four B-SOSE grid points (within 1° of the eastern boundary) probably due to the narrowness of the trench topography, shown in the companion study (X. Yang et al. 2020, unpublished manuscript) to play a prominent role in the dynamics of these currents. The southward transport itself is about 1 Sv and is almost fully compensated by the northward transport above the western flank of the trench (Fig. 3).

The DEBCs in B-SOSE are, of course, not as strong as the corresponding western boundary currents, and their magnitude is weaker than observations (Chretien and Speer 2019; Clement and Gordon 1995; Sloyan 2006). The simulated DEBCs do, however, show significant transports and nevertheless play a prominent role in setting the large-scale tracer distributions, motivating us to attempt to explain their dynamics.

3. Vorticity dynamics of deep eastern boundary currents

a. Regional model setup

We use the regional configurations of the Massachusetts Institute of Technology General Circulation Model (MITgcm; Marshall et al. 1997) to study the dynamics of these concentrated

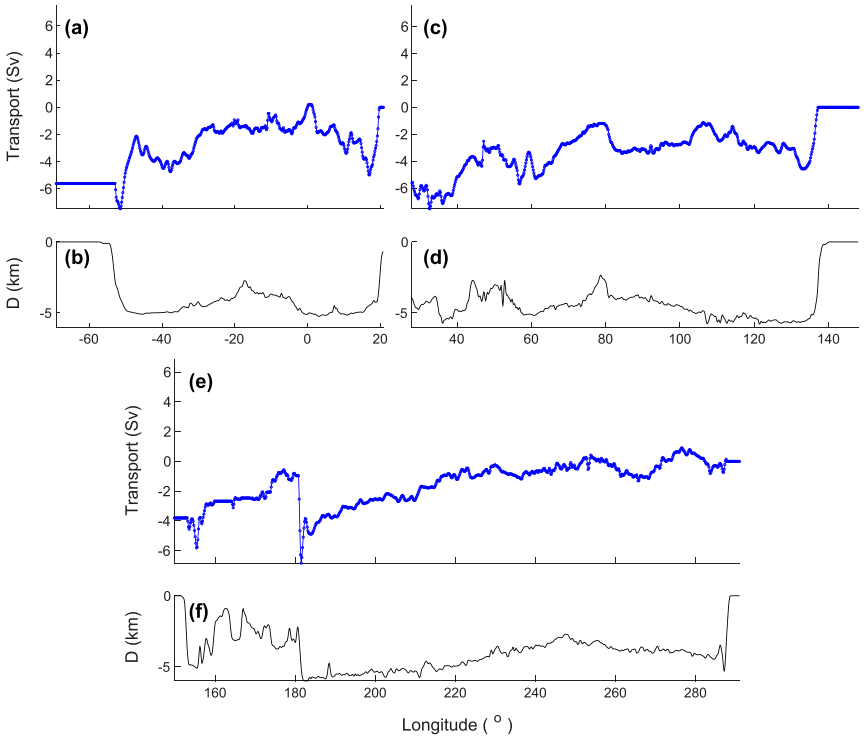

FIG. 4. Cumulative transports and corresponding bathymetry in the South Atlantic/Indian/Pacific Oceans (SOSE): (a),(b) South Atlantic Ocean (transport between 2.5 and 3.5 km at 37°S), (c),(d) south Indian Ocean (transport between 2.5 and 3.5 km, at 37°S), and (e),(f) South Pacific Ocean (transport between 2 and 3 km at 33°S).

southward deep eastern boundary currents in the southeastern Atlantic/Indian/Pacific Oceans, and this section summarizes the most important parameters of these regional experiments. We will refer to these MITgcm configurations as "regional" simulations to distinguish these runs from the SOSE analysis. The horizontal resolution is 0.1° and the vertical resolution varies from 5 m near the surface to 125 m near the bottom. Realistic bathymetry is used for each ocean basin (Fig. 8 of the online supplemental material).

In each experiment, the model is forced by restoring to monthly SST and SSS with a time scale of 7 days, and by monthly wind stress. These surface forcing data are interpolated from the Comprehensive Ocean–Atmosphere Dataset (COADS; Woodruff et al. 1987). The domains have open boundaries in the north, south and west where the monthly temperature/salinity/U/V/SSH from SOSE (Mazloff et al. 2010), averaged over six years (2005–10), are forced over prescribed sponge layers whose width is 20 grid points. We use boundary conditions from SOSE rather than B-SOSE due to the larger meridional extent of the SOSE domain which allows us to extend our regional domain equatorward. The restoring time scale of the open boundary conditions increases linearly from 20 days at the inner edge to one day at the outer edge. A no-slip boundary condition is used on the velocities at horizontal boundaries, following SOSE. The bottom boundary condition is of a linear bottom drag, with a coefficient of $10^{-3}\,\mathrm{s}^{-1}$, where the layer thickness is typically 125 m.

The vertical harmonic viscosity for these regional configurations is $A_r = 10^{-4}\,\mathrm{m}^2\,\mathrm{s}^{-1}$ (in the momentum this term is $A_r\partial_{zz}\mathbf{u}_h$), and the vertical diffusivity in the vertical tracer C mixing term, $\kappa_r\partial_{zz}C$, is $\kappa_r = 10^{-5}\,\mathrm{m}^2\,\mathrm{s}^{-1}$, as in SOSE. Because of the high resolution of the model, the strong surface wind forcing, and time-dependent boundary conditions, eddies are at least partially resolved in these experiments. Low values are therefore used for the horizontal viscosity, with $A_h = 10\,\mathrm{m}^2\,\mathrm{s}^{-1}$ in the momentum equation term $A_h\nabla_h^2\mathbf{u}_h$, and a Gent–McWilliams diffusivity of $\kappa_{\mathrm{GM}} = 10\,\mathrm{m}^2\,\mathrm{s}^{-1}$ (Gent and McWilliams 1990). For numerical stability, biharmonic diffusivity and viscosity are also used with $A_4 = \kappa_4 = 10^{10}\,\mathrm{m}^4\,\mathrm{s}^{-1}$, represented as $A_4\nabla_h^4\mathbf{u}_h$ and $\kappa_4\nabla_h^4C$ in the equations of momentum or tracers. In addition, a third-order direct-space–time flux-limiter advection scheme (MITgcm scheme 33) is used in the model.

The experiments are run for about 200 model years, until a statistical steady state is reached (layerwise averaged temperature and salinity converge), and the analysis is based on an additional 30 years beyond that point, over which time averages are calculated. All of the nonlinear terms discussed below are based on bidaily output data, averaged over 20 years.

b. DEBCs in the regional MITgcm simulations

The regional realistic configurations employed here for the Atlantic, Pacific, and Indian oceans, driven by inflow and outflow boundary conditions from SOSE, result in fairly

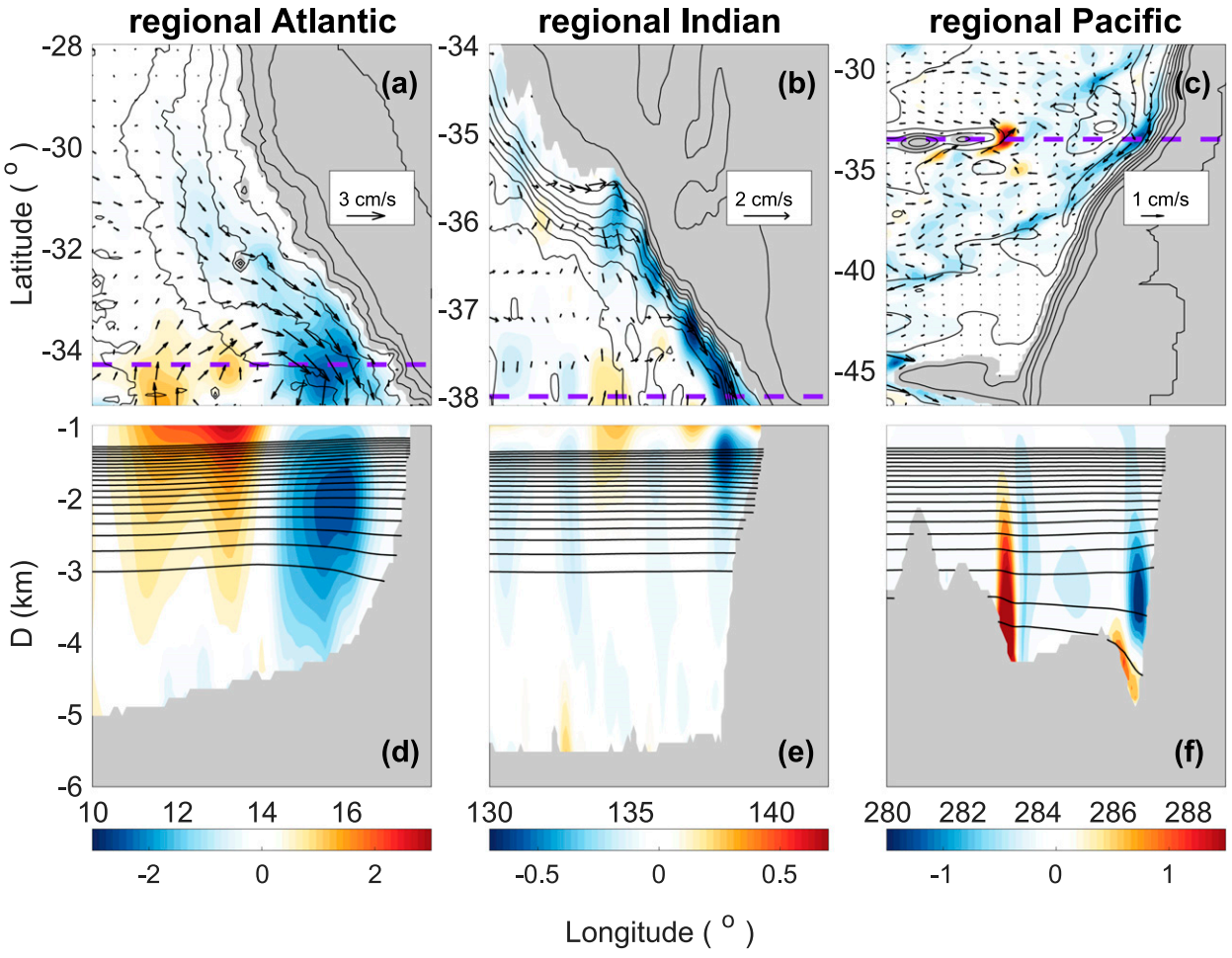

FIG. 5. DEBCs in the regional MITgcm simulations, with horizontal maps of northward velocity (color) and velocity vectors for the (a) southeastern Atlantic Ocean (depth = 2.5 km), (b) southeastern Indian Ocean (depth = 1.3 km), and (c) southeastern Pacific Ocean (depth = 3.2 km) and vertical sections of northward velocity (colors) and isopycnal surfaces (black contours, from 36.66 to 37.04 kg m^{-3}, with a 0.02 kg m^{-3} interval) for the (d) southeastern Atlantic Ocean (34.3°S), (e) southeastern Indian Ocean (38.0°S), and (f) southeastern Pacific Ocean (33.5°S). The dashed purple lines in (a)–(c) indicate the latitude at which the vertical sections are taken. Note that different color ranges are used for each regional simulation.

realistic-looking DEBCs. In the regional southeastern Atlantic simulation, a deep southward flow as strong as 3 cm s^{-1} is found starting at 32°S near the eastern boundary, extending southward. This current detaches from the boundary at 33°S but reattaches at higher latitude, and Figs. 5a and 5d show its core is at about 2–2.5-km depth at 34.3°S.

In the regional southeastern Indian Ocean run, concentrated eastern boundary currents are generally found at a shallower layer (1.5 km), comparable to the depth of the observed low oxygen cores in this region (Tamsitt et al. 2019). This is compatible with the outflow boundary condition interpolated from SOSE, but different from the DEBC in the B-SOSE assimilation product discussed earlier (Fig. 3) which is significantly deeper, at 3.5 km, indicating a sensitivity of the DEBC depth to model configuration. Using B-SOSE boundary conditions in our regional domain leads to a deeper DEBC, centered at 2 km depth and penetrating to 4 km (not shown). We choose to use SOSE because the northern boundary of B-SOSE is farther south (at 30°S vs 24.7°S of SOSE). In the South Australia Basin of the Indian Ocean, a DEBC starts at 36°S, fed by eastward flows at about 1.5-km depth (Figs. 5b,e). The regional model DEBC speed is about 2 cm s^{-1} (it appears smaller in the figure, about 0.7 cm s^{-1}, because the coast is tilted). The transport is about 0.4 Sv (divided into 0.36 Sv carried by the zonal velocity and 0.16 Sv by the meridional velocity). Other branches of the Indian Ocean DEBC are found at lower latitudes in our simulation (not shown), as well as in SOSE. The Indian Ocean DEBC has a similar vorticity budget to the DEBCs in the other two basins even though it is shallower.

In the regional southeastern Pacific Ocean simulation, concentrated southward flow starts at 32°S and ends at 38°S (Fig. 5c) when the current approaches the Chile Rise (Well et al. 2003). The fact that this DEBC is precisely above the Peru–Chile trench (Fig. 5f) and is accompanied by a recirculation to its west,

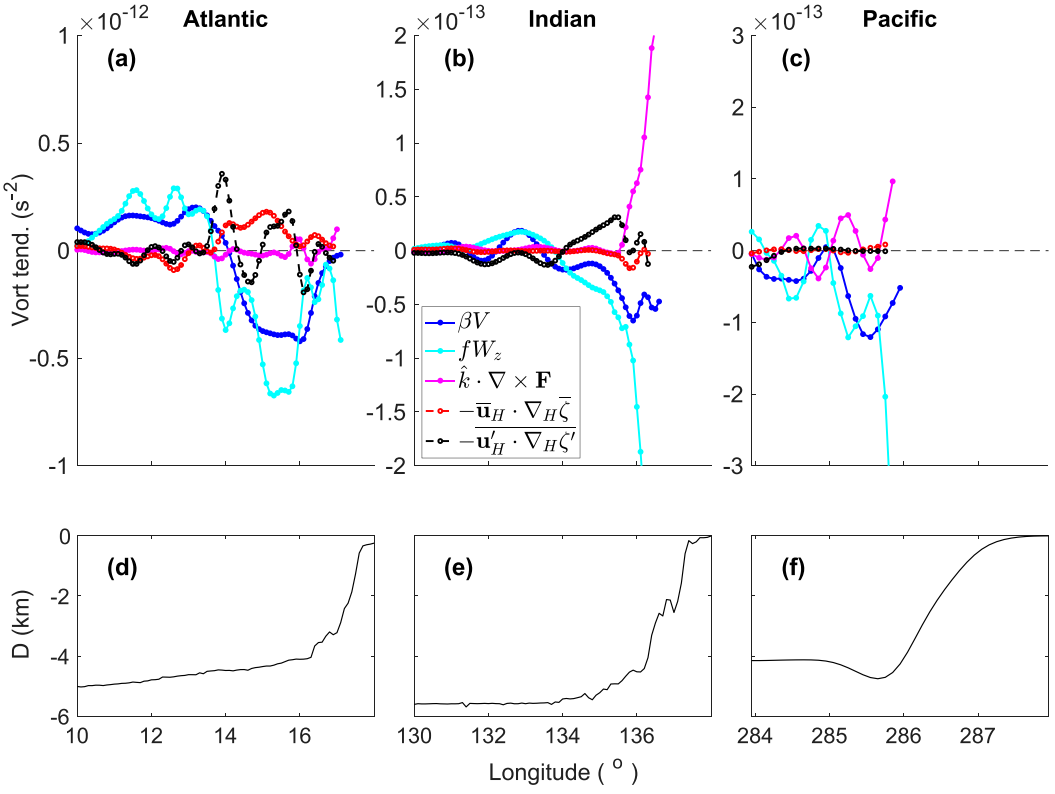

FIG. 6. (top) Vorticity budgets of the regional MITgcm simulations and (bottom) bathymetry profiles for the (a),(d) southeastern Atlantic Ocean (depth 2.5 km; 34.25°S); (b),(e) southeastern Indian Ocean (depth 1.3 km; 36.8°S); and (c),(f) southeastern Pacific Ocean (depth 3.8 km; 35.0°S).

suggests the important role played by topography in the dynamics of the Pacific DEBC (Johnson 1998). This is demonstrated in section 2 of the online supplemental material, where we remove the trench and show that the DEBC disappears, as well as in the companion study (X. Yang et al. 2020, unpublished manuscript) where we further explore the role of topography.

In summary, the regional MITgcm experiments forced by inflow and outflow boundary conditions interpolated from SOSE is able to simulate DEBCs in the southeastern Atlantic/Indian/Pacific Oceans that are comparable to the DEBCs in SOSE in terms of location and magnitude (Fig. 5). We therefore use these regional MITgcm results next to study the vorticity budget of the DEBCs (Fig. 6), that will, in turn, be used in the companion study (X. Yang et al. 2020, unpublished manuscript) to understand the detailed dynamics of these currents.

c. *Vorticity budget of DEBCs*

To understand the dynamics of the DEBCs, we now consider the time-averaged vorticity budget [Eq. (1)] of the DEBCs, for both our regional MITgcm experiments and SOSE, and the nonlinearity will be discussed in section 4a. The analysis is supplemented in a companion study (X. Yang et al. 2020, unpublished manuscript) by idealized GCMs and a simple vorticity model, in order to develop an understanding of the dynamics. The vorticity equation is obtained by taking the curl of the horizontal momentum equations,

$$\beta v = -\overline{\mathbf{u}_h} \cdot \nabla_h \overline{\zeta} - \overline{\mathbf{u}'_h \cdot \nabla_h \zeta'} - \overline{w} \partial_z \overline{\zeta} - \overline{w' \partial_z \zeta'} + f \partial_z w + \hat{k} \cdot \nabla \times \mathbf{F}. \quad (1)$$

All terms are evaluated in the spherical coordinates used by the MITgcm, where $\overline{(\,)}$ denotes a time average and $(\,)'$ is the departure from the time average; $\mathbf{u}$ is the horizontal velocity vector, v is meridional velocity, w is vertical velocity, and ζ is the vertical component of relative vorticity. Also, $f = 2\Omega \sin\theta$ is the Coriolis parameter, and β is the meridional gradient of f. In this equation, βv is the advection of planetary vorticity and $f\partial_z w$ is the vertical stretching term. The $-\overline{\mathbf{u}_h} \cdot \nabla_h \overline{\zeta}$ and $-\overline{\mathbf{u}'_h \cdot \boldsymbol{\zeta}'}$ are the horizontal advections by the mean flow and the eddies; $-\overline{w} \partial_z \overline{\zeta}$ and $-\overline{w' \partial_z \zeta'}$ are the advections of time-mean and eddy vertical velocity. The last term in the equation is the vertical component of the curl of friction. In general, we found that vertical advection terms are negligible compared to other processes in our regional simulations, and we exclude them in the following.

The vorticity budgets of the DEBCs in the southeastern Atlantic, Indian, and Pacific Oceans show some very prominent similarities between the regional runs and SOSE and between the different ocean basins. Across most of the width of the southward flow, including its western and central parts,

the balance is mainly between the beta term and vertical stretching ($\beta v \approx f\partial_z w$; blue and cyan curves in Fig. 6). This vorticity balance is thought to be important in the ocean interior, although it has been pointed out that this type of balance plays a role in the western boundary current (WBC) regions as well (Hughes and De Cuevas 2001; Jackson et al. 2006). Contributions from eddy vorticity advection are nonnegligible in the regional Atlantic and regional Indian cases, but of a smaller spatial scale. The temperature budget [see Eq. (1)] is analyzed to study the source of the vortex stretching term, and it reveals that in the DEBC regions, the vertical velocity is balanced by parameterized horizontal mixing (dominating the diffusion term shown in Fig. 15 of the online supplemental material) in the regional Pacific simulation [term ''diffusion'' in Eq. (1) in the online supplemental material], and by resolved eddy transports in the regional Atlantic and regional Indian simulations ($\overline{\mathbf{u}_h' \cdot \nabla_h T'}$). The resolved or parameterized temperature mixing is driven by horizontal temperature gradients due to the sloping isopycnals which are the result of the interaction between horizontal bottom flows and the bathymetry. In the companion study (X. Yang et al. 2020, unpublished manuscript), we find that the contribution of both bathymetry [the same as the ''pressure torque'' term in Hughes and De Cuevas (2001) and Jackson et al. (2006)] and temperature mixing to the stretching driving the meridional flow are comparable. The residual of the ''interior balance'' in each basin is dominated by parameterized friction very close to the eastern boundary and by nonlinear terms over the western and central parts of the DEBCs, to be discussed in section 4. The easternmost part of the DEBC has a different vorticity balance, where the friction and stretching terms grow dramatically toward the eastern boundary, and the β term is secondary in this region (Figs. 6a–c for the three ocean basins). This balance has been shown in the context of linear circulation in stratified rotating fluids to be needed to satisfy a no-slip boundary condition (Barcilon and Pedlosky 1967; LaCasce 2004; Gjermundsen and Lacasce 2017) and was referred to as the ''hydrostatic layer.'' While the DEBCs are generally stronger than the boundary currents discussed by Barcilon and Pedlosky (1967), that is the case only in an outer layer instead of in the frictional sublayer. A similar balance was also found in a study of the shallower eastern boundary current driven by meridional surface buoyancy gradients (Bire 2019; Wolfe and Bire 2019). A similar vorticity balance is also found in SOSE (Fig. 10 of the online supplemental material). It is possible that a ''free slip'' boundary condition, rather than the ''no slip'' used here, would have led to a different balance. Future studies will examine this issue at an even higher resolution, allowing resolved eddies to satisfy the boundary conditions instead of parameterized friction.

The vorticity balance described above holds at the depth of the core of the DEBCs, but varies with depth as shown in Fig. 7 for the regional experiments and in Fig. 11 of the online supplemental material for SOSE. At all depths, the balance over most of the width of the DEBC is the same ocean interior vorticity balance discussed above, $\beta v \approx f\partial_z w$. However, the signs of the strong growing trends in stretching and friction toward the eastern boundary are strongly depth dependent. In the Atlantic Ocean (Figs. 7a,d,g), the growing trend toward the eastern boundary appears only below the depth of the DEBC core. In the Indian and Pacific, they are seen both above and below, but both the friction and stretching terms reverse sign with depth (cf. Figs. 7b and 7i for the Indian and Figs. 7c and 7j for the Pacific). This vertical structure of the vorticity budget is shown in the companion study (X. Yang et al. 2020, unpublished manuscript) using a simple vorticity model to be a result of a near-Gaussian vertical structure of the current, combined with the upward tilting isopycnals above the core of the current and downward tilting isopycnals below. In general, the vorticity balances near the core depth of the DEBCs among the basins are similar.

4. Temporal variability of the deep eastern boundary currents

Although DEBCs clearly emerge in the three main Southern Hemisphere ocean basins in the time-averaged picture, the strong temporal variability near eastern boundaries can mask their signals in instantaneous observations. Knowledge of time variations of the DEBCs can therefore improve our ability to interpret observations in these regions. The DEBCs in both SOSE and the regional MITgcm simulations show strong temporal variability.

In the southeastern Pacific Ocean (both regional run and SOSE), the DEBC is persistently southward but its magnitude varies. In the southeastern Atlantic and Indian Oceans, the meridional velocity alternates in sign, even where southward DEBCs emerge in the time-averaged pictures. Considering the weakness of the time-averaged DEBCs and their strong temporal variability, the likelihood of these southward DEBCs being observed is evaluated using histograms representing the probability distribution function (pdf) of meridional velocities (Fig. 8). The pdf is for the spatially averaged meridional velocity over a one degree longitude range from the eastern boundary, at the characteristic depth and latitude of the time-averaged DEBC. The pdf is based on bidaily data over 20 years for the regional simulations, and on 5-day data over 6 years for SOSE.

It is clear from Fig. 8 that although the long-term time average shows a southward flow, the pdf for the meridional velocity in three ocean basins in SOSE and in the regional cases is broad, and in some cases apparently non-Gaussian. The probability to find instantaneous positive (equatorward) velocities is not negligible at these sites (Fig. 8). The probability of observing northward flows in the DEBC region in our regional Atlantic and Indian simulations is as large as 37.6% and 20.2%, consistent with the fact that the DEBCs in these experiments alternate in sign with time. In the regional Pacific simulation, the possibility of measuring northward flow is much lower but still not zero (Fig. 8c). This means that it is difficult to rely on occasional or one-time observations, especially in the southeastern Atlantic and Indian Oceans, and that a long-time average is necessary for these current to emerge, a greater challenge for observations.

We note that the simulated DEBC velocities from both SOSE and our regional simulations are generally weaker compared to observations. For example, in the southeastern

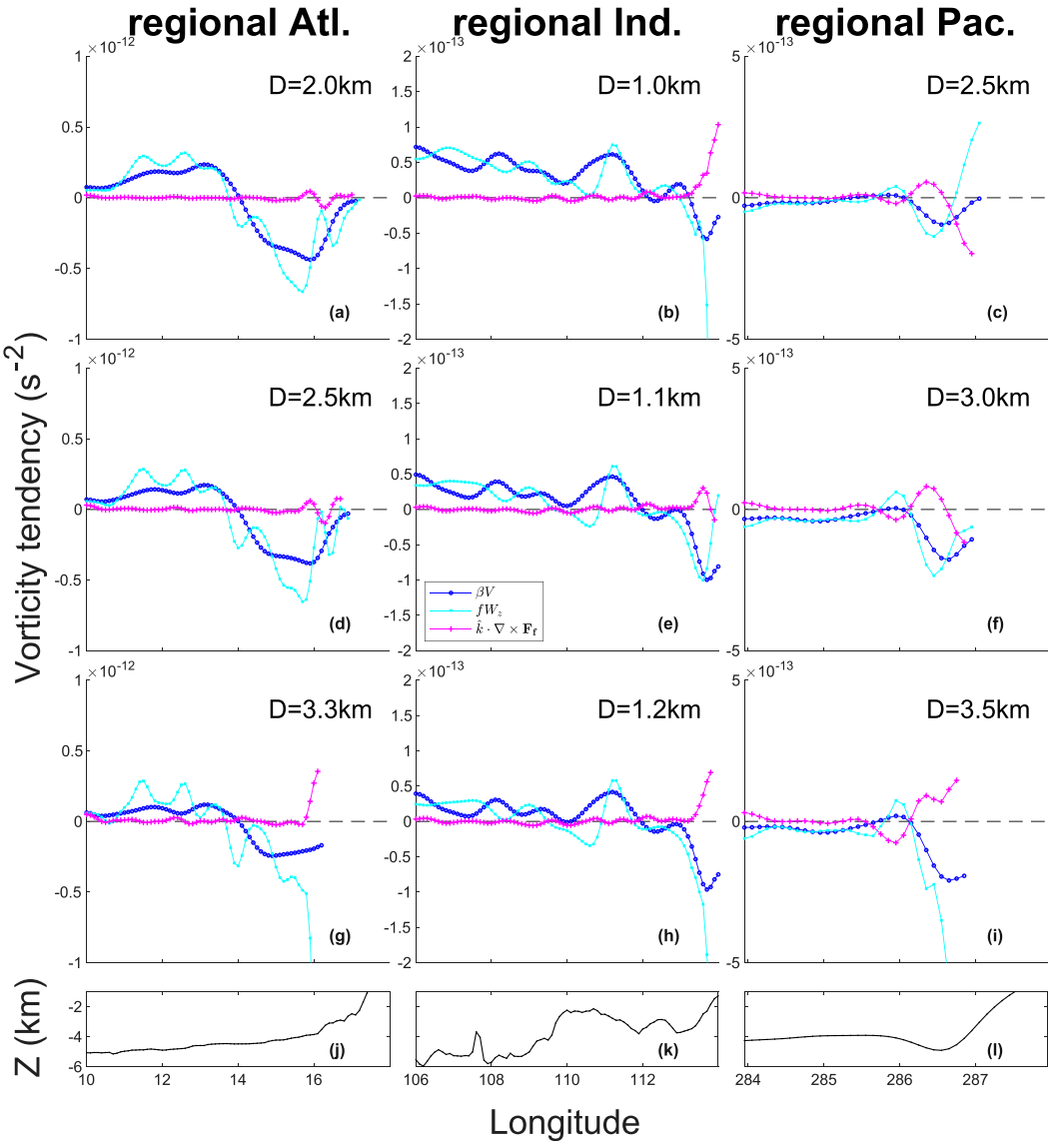

FIG. 7. Vorticity budgets at different depths in the regional MITgcm simulations for the (a),(d),(g) southeastern Atlantic Ocean (levels: 2, 2.5, and 3.0 km; latitude 33.5°S); (b),(e),(h) southeastern Indian Ocean (levels: 1.0, 1.1, and 1.2 km; latitude 33.4°S); and (c),(f),(i) southeastern Pacific Ocean (levels: 2.5, 3.0, and 3.5 km; latitude 33.5°S). Also shown are bathymetry profiles in the (j) southeastern Atlantic Ocean, (k) southeastern Indian Ocean, and (l) southeastern Pacific Ocean.

Pacific, core speeds as strong as 10 cm s^{-1} have been observed (Chretien and Speer 2019). In terms of transport, in the regional simulation, the meridional transport above the trench at 32.5°S between 2 and 4 km is 0.56 Sv southward, in comparison with 5 Sv in the 2010 observation of Chretien and Speer (2019), and 1.44 Sv in SOSE. Similarly, in the southeastern Indian Ocean, the core speed of the DEBC is observed to be about 10 cm s^{-1} with strong temporal variability (Sloyan 2006). Such strong currents are not simulated in SOSE or in our regional experiments. While the above discussion makes it clear that it is difficult to compare the sparse observations with long-term model averages, it seems that the stronger observed currents are outside of the range of velocities seen in SOSE and in the regional models, indicating model deficiencies.

We next (section 4a) discuss the role of eddy momentum fluxes in the momentum budget of the DEBCs, eddy vorticity transports, and the appearance of dominant westward-propagating signals emitted by the DEBCs (section 4b).

a. Eddy kinetic energy and the role of eddies in momentum and vorticity budgets

The strong eddies described in the previous section are important because they can mask the signals of DEBCs in observations, as noted above. In addition, eddy momentum fluxes

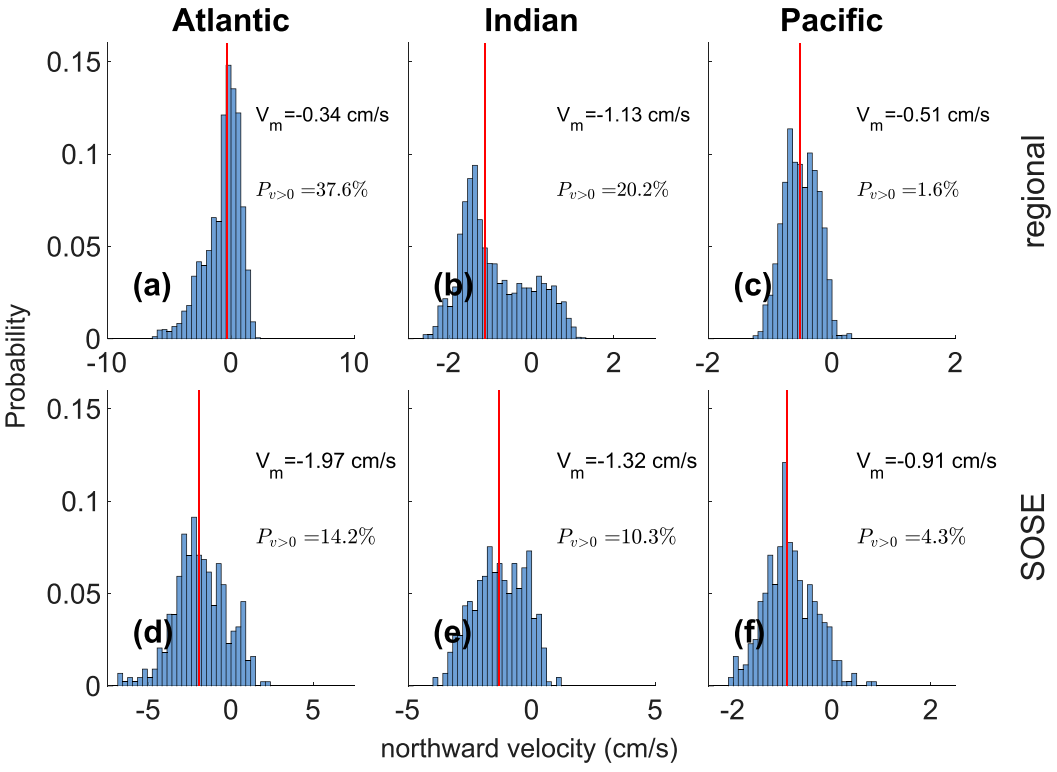

FIG. 8. Histograms of meridional velocity in the regional MITgcm simulations and for SOSE for (left) the Southeastern Atlantic Ocean (time series at 34.25°S and 3-km depth for regional runs and at 36.5°S and 3-km depth for SOSE); (center) the southeastern Indian Ocean (time series at 38°S and 1.5-km depth for regional runs and at 36°S and 1.8-km depth for SOSE), and (right) the southeastern Pacific Ocean (time series at 32.95°S and 3-km depth for regional runs and at 33°S and 3-km depth for SOSE) for (a)–(c) regional MITgcm experiments and (d)–(f) SOSE. The red vertical lines show the median velocity, also indicated as V_m; the shown $P_{v>0}$ values are the probability to observe a northward flow.

can help maintain jets (e.g., Ingersoll et al. 1981; Thompson and Richards 2011), and eddy induced velocities can contribute to tracer transports (based on the transformed Eulerian mean formulation; Plumb and Ferrari 2005; Vallis 2017). The eddy-induced velocities and the relationship to the Eulerian velocities are presented in section 5 of the online supplemental material (supplemental Figs. 16–18), where we show that the horizontal eddy-induced velocities in the three DEBC regional simulations are very weak compared with the mean Eulerian flows, but the eddy-induced vertical velocities are comparable to the mean Eulerian ones.

The square root of 2 times the eddy kinetic energy, $(\overline{u'^2 + v'^2})^{1/2}$, reflecting the magnitude of the eddy velocities, is plotted for the three regional experiments in Fig. 9. In the regional southeastern Atlantic run (Figs. 9a,d), there is a patch of high eddy kinetic energy to the west and above the core of the current. This signal is related to the Agulhas rings that affect the SOSE-derived time-dependent southern boundary conditions used here (section 3a). The core of the DEBC shows a lower eddy kinetic energy compared to that just west of the DEBC.

In the regional southeastern Indian case (Figs. 9b,e) there is also a patch of high eddy kinetic energy to the west of the core of the current. The core of the DEBC in the southeastern Indian Ocean is closer to the high center of the eddy kinetic energy than it is in the southeastern Atlantic Ocean. Yet the vertical section in Fig. 9e shows the DEBC core still has a comparatively low eddy kinetic energy. It is very clear that the core of the DEBC in the regional southeastern Pacific run, shown in Figs. 9c and 9f, has very low eddy kinetic energy as well. Overall, in the regional experiments, eddy activity in the southeastern Atlantic Ocean is the strongest; it is weakest in the southeastern Pacific Ocean. The eddy velocity magnitudes seen in the regional Atlantic and Indian simulations are consistent with the sign changes of the meridional flow in these regions noted above. In summary, in the regional simulations, the cores of DEBCs in the southeastern Atlantic, Indian, and Pacific Oceans experience a low eddy kinetic energy, consistent with observations in the southeastern Pacific Ocean (Shaffer et al. 1995).

The eddy energy distributions and their relation to the location of the DEBC are consistent between the regional experiments and SOSE (cf. Fig. 9 and online supplemental Fig. 13). Overall, eddy kinetic energy in SOSE is higher than in the regional simulations, although the resolution of the regional simulations is higher and the same time-dependent surface forcings and horizontal boundary conditions are used,

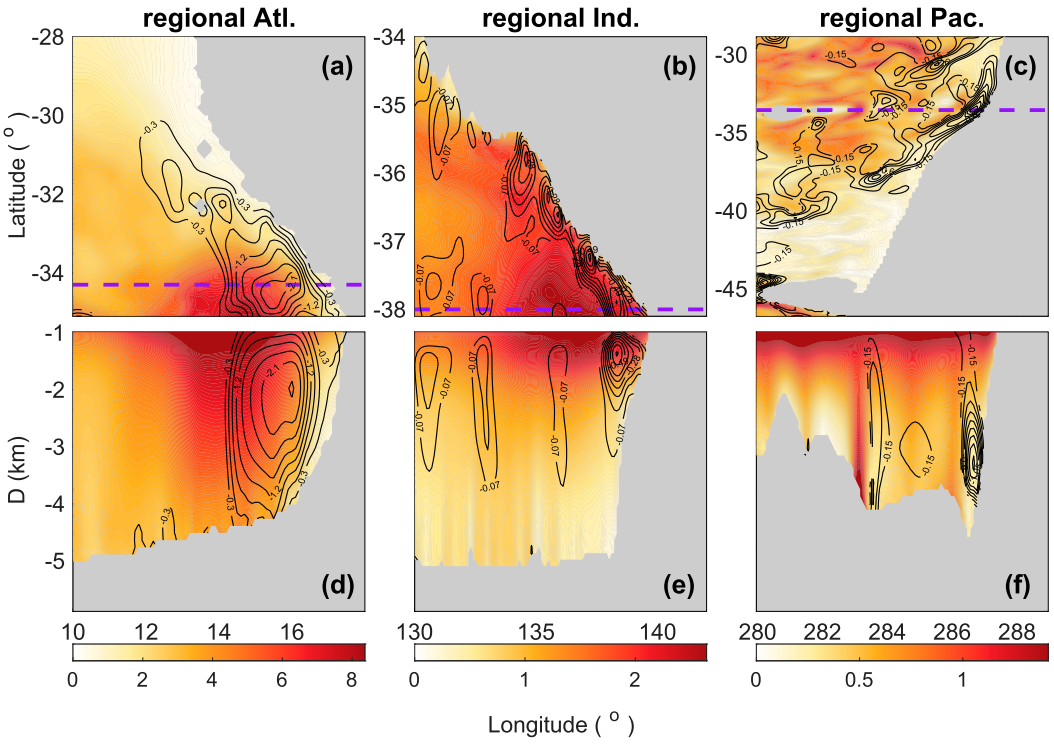

FIG. 9. Eddy velocity magnitudes $[V_E \equiv (u'^2 + v'^2)]^{1/2}$, with horizontal maps of V_E (colors; cm s^{-1}) and time-mean meridional velocity (black contours; cm s^{-1}) in the (a) southeastern Atlantic Ocean (at a depth of 2.5 km), (b) southeastern Indian Ocean (1.3 km), and (c) southeastern Pacific Ocean (3.2 km) and vertical sections of V_E (color) and southward time-mean velocity (black contours) in the (d) southeastern Atlantic Ocean (34.2°S), (e) southeastern Indian Ocean (38°S), and (f) southeastern Pacific Ocean (33.5°S). The dashed purple lines in (a)–(c) indicate the latitude at which the vertical sections are taken. Note that different color ranges are used for different ocean basins.

as well as the same eddy coefficients. It is possible that the stronger eddy activity in SOSE is due to the short time of its integration: this might not allow a statistical steady state to develop, and the averaged eddy activity over six years may be too short to be representative of the climatology. Alternatively, the SOSE boundary conditions used here may not be able to effectively represent the propagation of eddies into the regional domains.

Eddy momentum transport is often an important mechanism for the maintenance of a concentrated jet (Ingersoll et al. 1981; Thompson and Richards 2011). We find that the eddy momentum flux term $\overline{u'v'}$ is negative in the DEBC region in the regional Atlantic and Indian simulations (Figs. 20 and 21 in the online supplemental material). In the regional Pacific simulation, the branch of DEBC at lower latitudes shows very weak eddy momentum transport (supplemental Figs. 20 and 21), but the high-latitude branch behaves similarly to the other two regional simulations (not shown).

Consider the divergence of these eddy fluxes, which determines the acceleration of the mean flows—in particular, the v-momentum budget:

$$\partial_t \overline{v} = -\partial_y \overline{p} - f\overline{u} - \nabla_h \cdot \overline{\mathbf{u}}_h \overline{v} - \nabla_h \cdot \overline{\mathbf{u}'_h v'} - \partial_z \overline{w}\,\overline{v} - \partial_z \overline{w'v'} + F_y.$$

Figure 10 shows the horizontal divergence of the eddy transport of meridional momentum, $-\nabla_h \cdot \overline{\mathbf{u}'_h v'}$, representing the time-mean momentum tendency due to the eddies. In the regional southeastern Atlantic simulation (Figs. 10a,d) the eddy-driven v-momentum tendency is positive in the DEBC region. Given that the mean velocity is negative (southward), this means that eddy momentum flux divergence acts as a drag on the time-mean southeastern Atlantic DEBC. The same conclusion can be drawn for the regional southeastern Indian case (Figs. 10b,e). As indicated by the small eddy velocity magnitudes shown above for the regional southeastern Pacific, contributions from the eddy v-momentum transport to the DEBC momentum balance there are negligible (Figs. 10c,f). In SOSE, the relationship between DEBC and eddy momentum transport is similar to that in the regional MITgcm simulations for the southeastern Atlantic and Indian Oceans. At 49°S in the southeastern Pacific, though, eddy momentum tendency is nonnegligible, again acting as a drag on the mean flow.

An analysis of the Lorenz energy cycle averaged over the DEBC region, shows that while the transfer is from mean to eddy kinetic energy at shallower layers, it is from eddy to mean kinetic energy at depth (Fig. 19 in the online supplemental material), consistent with von Storch et al. (2012). In both the

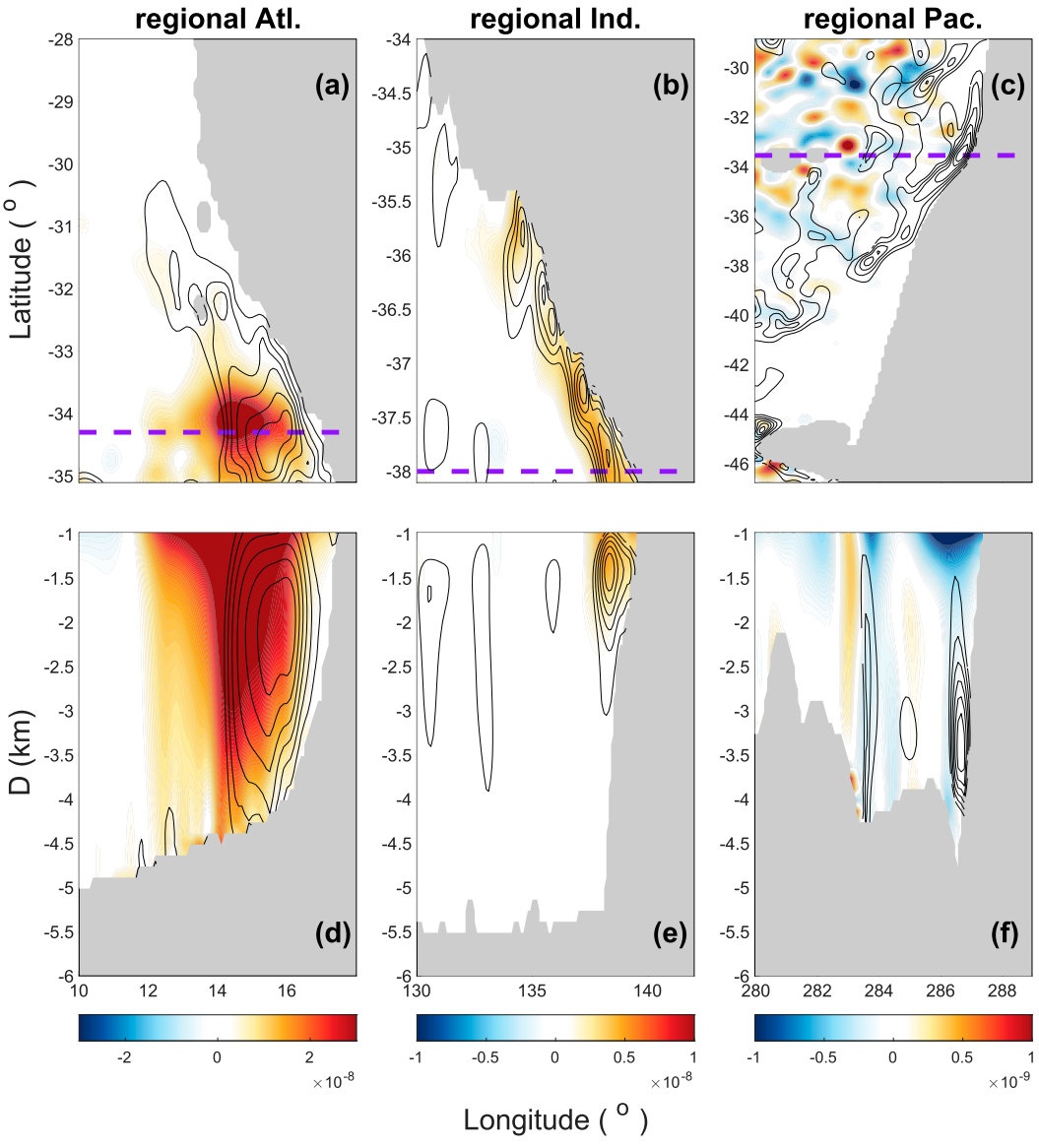

FIG. 10. Eddy momentum flux divergence in the meridional momentum equation ($-\nabla_h \cdot \overline{\mathbf{u}'v'}$, including both diagonal and off-diagonal eddy stress elements) for the regional MITgcm experiments for (top) horizontal and (bottom) vertical sections for the (a),(d) southeastern Atlantic Ocean (depth: 2.5 km; latitude: 34°S); (b),(e) southeastern Indian Ocean (depth: 1.3 km; latitude: 38°S); and (c),(f) southeastern Pacific Ocean (depth: 3.2 km; latitude: 33.5°S). The dashed purple lines in (a)–(c) indicate the latitude at which the vertical sections are taken. Different color ranges are used for different regional simulations.

regional Indian and Pacific simulations, the transfer near the DEBC core is from eddy to mean kinetic energy, while in the regional Atlantic the eddies extract energy from the mean flow near the DEBC core, but transform to mean flow energy only deeper than 3.5 km.

We now move to a discussion of eddy effects in the vorticity budget. As mentioned in section 3c, the linear terms in the vorticity Eq. (1) behave similarly in the different ocean basins. The role played by the nonlinear terms, however, is different in the different oceans. In the regional southeastern Atlantic Ocean simulation (Figs. 6a,d), in the western part of the DEBC region (between 14° and 16°E), vorticity advection by eddies and mean flow (red and black curves) are both nonnegligible. To the east (between 15° and 18°E), mean flow advection is small but the contribution by eddies is larger and negative (Fig. 6a). This implies that the eddy transport of relative vorticity tends to balance a beta term corresponding to a southward flow, like the stretching term, and opposite to friction. Over the western part of the southward DEBC, the mean vorticity advection balances a northward flow while the contribution of eddies depends on longitude. At the western edge of the DEBC and its interior the eddy vorticity transport

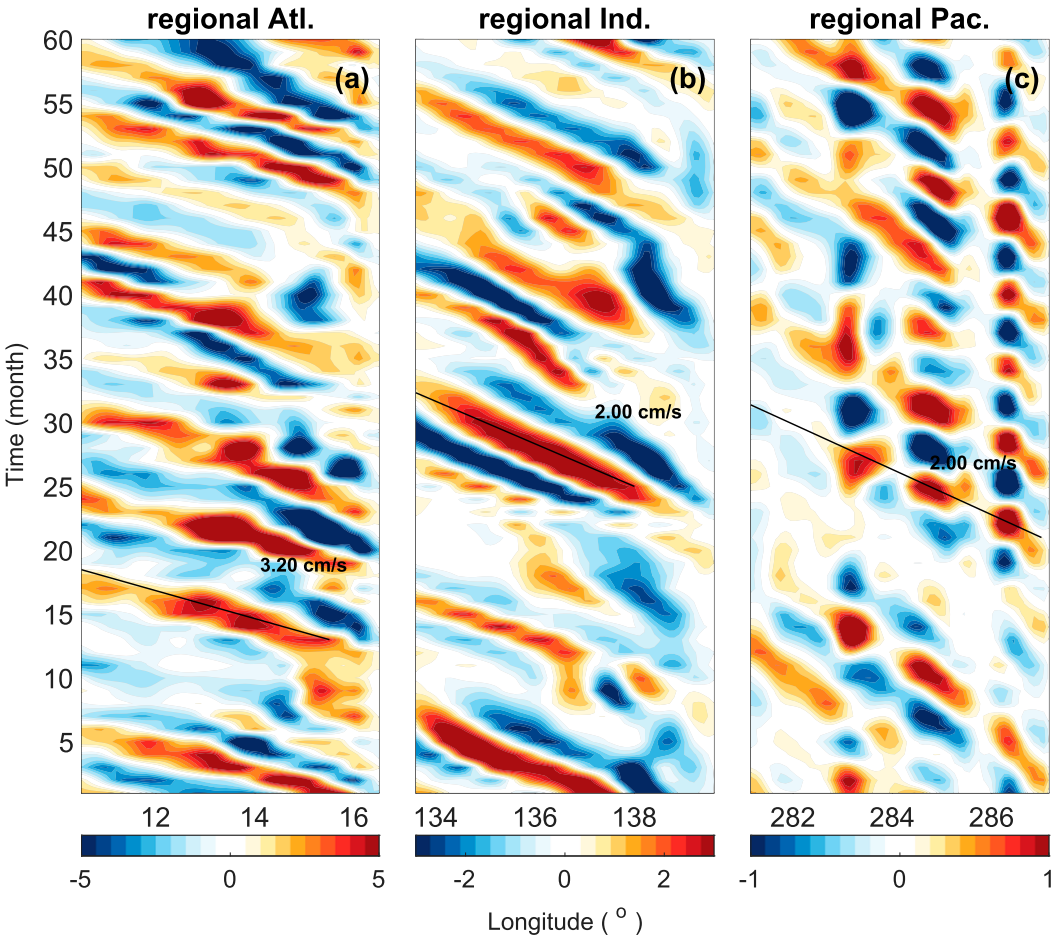

FIG. 11. Hovmöller diagrams of meridional velocity anomalies from the regional MITgcm experiments for the (a) southeastern Atlantic Ocean (at 3-km depth), (b) southeastern Indian Ocean (at 1.5-km depth), and (c) southeastern Pacific Ocean (at 3-km depth).

counteracts the southward flow, but between 14° and 15°E it enhances the DEBC. In the regional southeastern Indian Ocean run, the contribution of mean flows and eddies both enhance a southward flow very close to the eastern boundary, but their effect is weak in this region (east of 135°E). However, in the western part of the DEBC, eddy transport is non-negligible and positive, tending to brake the southward flow (Fig. 6b). Nonlinearity is small everywhere in the regional southeastern Pacific run vorticity budget (Fig. 6c), and in the companion study (X. Yang et al. 2020, unpublished manuscript) we use a linear vorticity model motivated in particular by this prominent and simpler DEBC case to show the key role played by temperature mixing and topography in driving vortex stretching. We note that the behavior of the nonlinear terms in the vorticity budget in SOSE agrees with the above results (Fig. 10 of the online supplemental material).

Throughout our study, the roles of resolved or parameterized eddies in the temperature, momentum and vorticity budgets were examined. Eddy temperature transport was found important in driving the vertical stretching which dominates the vorticity budget of the DEBCs, together with the beta term, over most of their width. We find that eddy momentum flux divergence systematically acts to slow the currents down, while the effects of nonlinear eddy advection in the vorticity budget are not consistent for the different DEBCs. For the regional Atlantic case the effect of eddies on the vorticity budget varies with longitude, and in the regional Indian case it generally balances a beta term corresponding to northward mean flow. More generally, eddy terms in the momentum and vorticity equations represent different effects that are difficult to directly compare: in the momentum budget, the eddy terms contribute to the acceleration, whereas in the vorticity budget the nonlinear advection terms (arising from the curl of the momentum advection) affect the southward DEBC velocity v via the beta term.

b. Wave activity associated with the deep eastern boundary currents

Figure 11 shows the Hovmöller diagram of the northward velocity anomaly from its time mean over five years in southeastern Atlantic, Indian, Pacific oceans from the regional MITgcm simulations. It clearly shows signals propagating

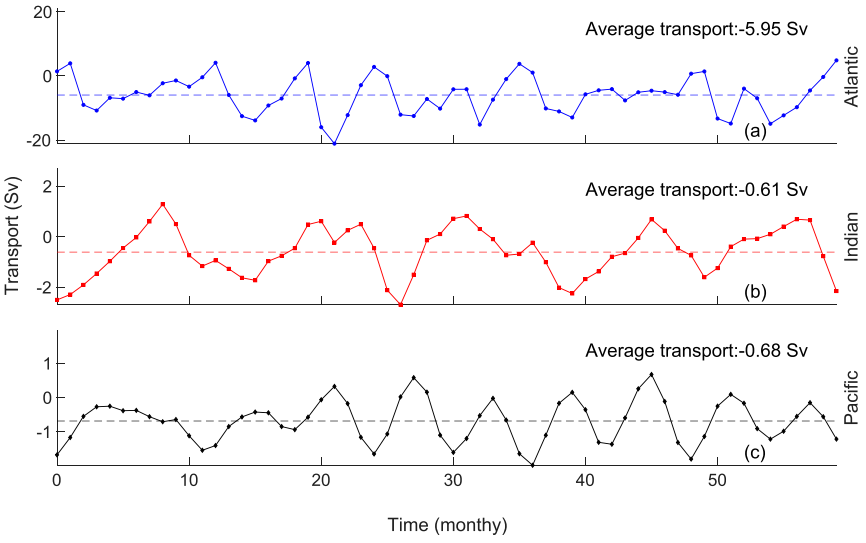

FIG. 12. Time series of the meridional transport in the region where time-averaged DEBCs emerge in the regional MITgcm experiments for the (a) Atlantic Ocean east of 14°E, at 34°S, and between 2- and 4-km depth; (b) Indian Ocean east of 138°E, at 37.95°S, and between 1- and 2-km depth; and (c) Pacific Ocean east of 286°E, at 33.5°S, and between 2- and 4-km depth. Dashed lines show the time-averaged transports.

westward away from the eastern boundaries in the three ocean basins, likely stimulated by the temporal variability of the DEBCs (Fig. 12). Phase speeds evaluated from the Hovmöller diagrams are 3.2, 2.0, and 2.0 cm s^{-1} for the southeastern Atlantic/Indian/Pacific Oceans, respectively. Similar phase speeds are observed for SOSE (Fig. 11 of the online supplemental material).

The propagating signals have a surface-intensified vertical structure, with significant signal at the DEBC depths (not shown), and their westward propagation is indeed well explained as Rossby waves with a phase speed of

$$c = \frac{-\beta}{k^2 + l^2 + L_d^{-2}}, \tag{2}$$

where $\beta = 2\Omega \cos\theta/R$, k is the zonal wavenumber, l is the meridional wavenumber, and L_d is the internal Rossby deformation radius.

The zonal and meridional wavenumbers are determined via spectral analysis of the regional GCM simulations (not shown), according to which the meridional wavelengths are generally much larger compared to the zonal wavelengths, therefore making a negligible contribution to Rossby wave phase speed [Eq. (2)]. For the southeastern Atlantic Ocean, for example, at 34°S and 3-km depth, the zonal wavelength is found to be 460 km and the meridional one is 3–4 times as large. A deformation radius of 42 km results in the best fit of the Rossby wave phase speed to the observed propagation speed in the simulation (black line in Fig. 11a). Similarly, in the southeastern Indian Ocean, at 37.5°S and 1.5-km depth, the zonal wavelength is 440 km, while the best-fit Rossby deformation radius is 40 km. For the southeastern Pacific Ocean, the Rossby waves have a zonal wavelength of 233 km and the best-fit deformation radius is 59 km. The separation between the zonal wavelength and the Rossby deformation radius means that this wave speed is close to that of the nondispersive long Rossby wave.

We note that the vertical structure of the Rossby waves is quite different from that of the DEBCs, and the two can be distinguished from one another in observations with sufficient temporal and vertical resolutions. But in any case, the Rossby waves still strongly project on the horizontal and vertical structures of these currents, with the observational consequences discussed above.

5. Conclusions

Concentrated poleward deep eastern boundary currents have been repeatedly observed between 2 and 4 km in the southeastern Atlantic, Indian, and Pacific Oceans. In this work, the first of a two-part study of the DEBCs, we study the tracer distributions, mass transport and vorticity budgets of DEBCs in the Atlantic, Pacific, and Indian Oceans, using the SOSE data assimilation product and realistic regional GCM configurations. The companion study (X. Yang et al. 2020, unpublished manuscript) discusses the dynamics of DEBCs using both idealized GCM configurations and theoretical models. Such currents are simulated in SOSE, and their transports are found to be nonnegligible, even in comparison with the transport of deep western boundary currents. However, DEBCs may not seem strong, and they are often accompanied by a neighboring recirculation. Our first goal here, therefore, was to demonstrate that these currents play a prominent role in long-term averaged tracer distributions. We analyzed tracer distributions (dissolved inorganic carbon, phosphate, oxygen, temperature and salinity), from the data assimilation product B-SOSE (Verdy and Mazloff 2017), which show tongue-like structures near these eastern boundary currents, showing the signatures of water masses

of northern characteristics, indicating concentrated southward flows near the eastern boundaries, and confirming the importance of DEBCs to large-scale property transport.

We then used regional high-resolution configurations of the MITgcm, forced by time-dependent lateral boundary conditions derived from SOSE, to study the DEBCs in these three oceans. Our regional configurations successfully simulated poleward DEBCs at the right location and depth, although with slightly weaker magnitudes compared with SOSE, possibly because that better resolved eddies in the regional simulations slow the currents down. We use these realistic eddy resolving regional simulations to study the vorticity budget of DEBCs. We find that the DEBC vorticity dynamics are different from those of shallower eastern boundary currents, where various trapping mechanisms were proposed to explain their proximity to the boundary [as is further discussed, with detailed references, in the companion study (X. Yang et al. 2020, unpublished manuscript)]. The DEBC vorticity balance is consistently found to be between planetary vorticity advection and vertical stretching ($\beta v = f w_z$) over most of the width of the DEBCs in all three oceans, a typical balance one expects in the ocean interior [but also found in the regions of western boundary currents by Hughes and De Cuevas (2001) and Jackson et al. (2006)]. Very close to the eastern boundary, though, strong compensating vorticity trend signals are observed, between friction and stretching, growing toward the boundary. As we explain in the companion study (X. Yang et al. 2020, unpublished manuscript), this special boundary layer balance has been proposed before (Barcilon and Pedlosky 1967; LaCasce 2004; Gjermundsen and Lacasce 2017; Bire 2019; Wolfe and Bire 2019), to satisfy the no parallel flow boundary condition at the eastern boundary.

The DEBCs in SOSE and our regional simulations show a strong temporal variability that may mask the signal of the time-averaged southward flows in observations. One of our goals in this paper, therefore, is to provide some perspective on the time variability, which may help to interpret the sporadic observations mostly representing a one-time snapshot rather than a time-averaged picture. We find in the realistic regional simulations strong signals originating from the DEBCs and propagating westward. The PDF of the meridional velocities near the eastern boundary is wide, implying a significant probability to observe both poleward and reversed (equatorward) velocities in the DEBC regions, making it a challenge to observe these currents. On the other hand, the DEBCs are found to reside in areas of relatively low eddy kinetic energy.

The roles of resolved or parameterized eddies in the temperature, momentum and vorticity budgets were examined throughout this study. Eddy temperature transport was found important in driving the vertical stretching which dominates the vorticity budget of the DEBCs, together with the beta term, over most of their width, while eddy momentum flux divergence systematically acts to slow the currents down, unlike the case of the Southern Ocean jets (Thompson and Richards 2011), for example. The effects of nonlinear eddy advection in the vorticity budget are not consistent for the different DEBCs.

There are some important caveats to note. The core speeds of the DEBCs, both from SOSE and our simulations, are significantly weaker than some observed velocities, and the reason for this is still unclear. Also, our high-resolution model configurations for the three oceans are regional, and interaction with other parts of the global ocean that may be important are missing, such as waves and eddies that may propagate into the DEBC domain. Additionally, we have specified the inflows and outflows of the DEBCs here, but the source and dynamics of the inflows/outflows will need to be addressed in future work. The boundary conditions come from SOSE, which is integrated over a relatively short time of a few years, and may not reflect the climatological boundary conditions, although they do lead to successful DEBC simulations in our regional model configurations.

In summary, we evaluate and confirm the important role played by the deep eastern boundary currents in terms of mass and tracer transports based on SOSE, and on realistic regional GCM simulations, and study their vorticity budgets in the southeastern Atlantic, Indian and Pacific Oceans. In the companion study (X. Yang et al. 2020, unpublished manuscript) we elaborate on the dynamics using idealized GCM simulations and a simple semi-analytical vorticity models.

Acknowledgments. We thank the reviewers for their knowledgeable and helpful comments. Authors Yang and Tziperman are supported by the National Science Foundation Physical Oceanography Program, Grant OCE-1535800. Author Speer is supported by NSF OCE-1536045. We acknowledge high-performance computing support from Cheyenne provided by NCAR's Computational and Information Systems Laboratory, sponsored by the National Science Foundation. Tziperman thanks the Weizmann Institute for its hospitality during parts of this work. The authors declare no conflict of interests.

Data Availability Statement. The MITgcm 3D ocean model used for this work is a community-developed model available online for download (http://mitgcm.org/public/source_code.html). All data, MITgcm modifications, vorticity model codes, and analysis scripts used in this work are archived in the ''Open Science Framework,'' which is a public, community-supported, repository (https://osf.io/agtmq/). These codes are publicly available, with no restrictions. Southern Ocean State Estimate Dataset used in this paper can be found at http://sose.ucsd.edu.World Ocean Circulation Experiment (WOCE) data were used in this paper; the LADCP data can be found at https://currents.soest.hawaii.edu/clivar/ladcp/, and the tracer data can be found at https://cchdo.ucsd.edu/.

REFERENCES

Arhan, M., H. Mercier, and Y.-H. Park, 2003: On the deep water circulation of the eastern South Atlantic Ocean. *Deep-Sea Res. I*, **50**, 889–916, https://doi.org/10.1016/S0967-0637(03)00072-4.

Barcilon, V., and J. Pedlosky, 1967: A unified linear theory of homogeneous and stratified rotating fluids. *J. Fluid Mech.*, **29**, 609–621, https://doi.org/10.1017/S0022112067001053.

Bire, S., 2019: Eddy dynamics of eastern boundary currents. Ph.D. thesis, Stony Brook University, 132 pp.

Chretien, L. M. S., and K. Speer, 2019: A deep eastern boundary current in the Chile Basin. *J. Geophys. Res. Oceans*, **124**, 27–40, https://doi.org/10.1029/2018JC014400.

Clement, A. C., and A. L. Gordon, 1995: The absolute velocity field of Agulhas eddies and the Benguela Current. *J. Geophys. Res.*, **100**, 22 591–22 601, https://doi.org/10.1029/95JC02421.

Faure, V., and K. Speer, 2012: Deep circulation in the eastern South Pacific Ocean. *J. Mar. Res.*, **70**, 748–778, https://doi.org/10.1357/002224012806290714.

Gent, P. R., and J. C. McWilliams, 1990: Isopycnal mixing in ocean circulation models. *J. Phys. Oceanogr.*, **20**, 150–155, https://doi.org/10.1175/1520-0485(1990)020<0150:IMIOCM>2.0.CO;2.

Gjermundsen, A., and J. H. Lacasce, 2017: Comparing the linear and nonlinear buoyancy-driven circulation. *Tellus*, **69A**, 1299282, https://doi.org/10.1080/16000870.2017.1299282.

Hickey, B. M., 1979: The California Current system—Hypotheses and facts. *Prog. Oceanogr.*, **8**, 191–279, https://doi.org/10.1016/0079-6611(79)90002-8.

Hogg, N. G., and A. M. Thurnherr, 2005: A zonal pathway for NADW in the South Atlantic. *J. Oceanogr.*, **61**, 493–507, https://doi.org/10.1007/s10872-005-0058-7.

Hughes, C. W., and B. A. De Cuevas, 2001: Why western boundary currents in realistic oceans are inviscid: A link between form stress and bottom pressure torques. *J. Phys. Oceanogr.*, **31**, 2871–2885, https://doi.org/10.1175/1520-0485(2001)031<2871:WWBCIR>2.0.CO;2.

Ingersoll, A. P., R. F. Beebe, J. L. Mitchell, G. W. Garneau, G. M. Yagi, and J.-P. Müller, 1981: Interaction of eddies and mean zonal flow on Jupiter as inferred from Voyager 1 and 2 images. *J. Geophys. Res. Space Phys.*, **86**, 8733–8743, https://doi.org/10.1029/JA086iA10p08733.

Jackson, L., C. W. Hughes, and R. G. Williams, 2006: Topographic control of basin and channel flows: The role of bottom pressure torques and friction. *J. Phys. Oceanogr.*, **36**, 1786–1805, https://doi.org/10.1175/JPO2936.1.

Johnson, G. C., 1998: Deep water properties, velocities, and dynamics over ocean trenches. *J. Mar. Res.*, **56**, 329–347, https://doi.org/10.1357/002224098321822339.

LaCasce, J., 2004: Diffusivity and viscosity dependence in the linear thermocline. *J. Mar. Res.*, **62**, 743–769, https://doi.org/10.1357/0022240042880864.

Marshall, J., A. Adcroft, C. Hill, L. Perelman, and C. Heisey, 1997: A finite-volume, incompressible Navier Stokes model for studies of the ocean on parallel computers. *J. Geophys. Res.*, **102**, 5753–5766, https://doi.org/10.1029/96JC02775.

Mazloff, M. R., P. Heimbach, and C. Wunsch, 2010: An eddy-permitting Southern Ocean state estimate. *J. Phys. Oceanogr.*, **40**, 880–899, https://doi.org/10.1175/2009JPO4236.1.

Munk, W. H., 1950: On the wind-driven ocean circulation. *J. Meteor.*, **7**, 80–93, https://doi.org/10.1175/1520-0469(1950)007<0080:OTWDOC>2.0.CO;2.

Nelson, G., 1989: Poleward motion in the Benguela area. *Poleward Flows along Eastern Ocean Boundaries*, Springer, 110–130.

Peliz, Á., J. Dubert, D. B. Haidvogel, and B. Le Cann, 2003: Generation and unstable evolution of a density-driven Eastern Poleward Current: The Iberian Poleward Current. *J. Geophys. Res.*, **108**, 3268, https://doi.org/10.1029/2002JC001443.

Plumb, R. A., and R. Ferrari, 2005: Transformed Eulerian-mean theory. Part I: Nonquasigeostrophic theory for eddies on a zonal-mean flow. *J. Phys. Oceanogr.*, **35**, 165–174, https://doi.org/10.1175/JPO-2669.1.

Robbins, P. E., and J. M. Toole, 1997: The dissolved silica budget as a constraint on the meridional overturning circulation of the Indian Ocean. *Deep-Sea Res. I*, **44**, 879–906, https://doi.org/10.1016/S0967-0637(96)00126-4.

Shaffer, G., S. Salinas, O. Pizarro, A. Vega, and S. Hormazabal, 1995: Currents in the deep ocean off Chile (30°S). *Deep-Sea Res. I*, **42**, 425–436, https://doi.org/10.1016/0967-0637(95)99823-6.

——, S. Hormazabal, O. Pizarro, and M. Ramos, 2004: Circulation and variability in the Chile basin. *Deep-Sea Res. I*, **51**, 1367–1386, https://doi.org/10.1016/j.dsr.2004.05.006.

Sloyan, B. M., 2006: Antarctic bottom and lower circumpolar deep water circulation in the eastern Indian Ocean. *J. Geophys. Res.*, **111**, C02006, https://doi.org/10.1029/2005JC003011.

——, and S. R. Rintoul, 2001: The Southern Ocean limb of the global deep overturning circulation. *J. Phys. Oceanogr.*, **31**, 143–173, https://doi.org/10.1175/1520-0485(2001)031<0143:TSOLOT>2.0.CO;2.

Speer, K. G., G. Siedler, and L. Talley, 1995: The Namib Col Current. *Deep-Sea Res. I*, **42**, 1933–1950, https://doi.org/10.1016/0967-0637(95)00088-7.

Stommel, H., 1948: The westward intensification of wind-driven ocean currents. *Trans. Amer. Geophys. Union*, **29**, 202–206, https://doi.org/10.1029/TR029i002p00202.

——, and A. B. Arons, 1960: On the abyssal circulation of the world ocean. II. an idealized model of the circulation pattern and amplitude in oceanic basins. *Deep-Sea Res.*, **6**, 217–233, https://doi.org/10.1016/0146-6313(59)90075-9.

Tamsitt, V., and Coauthors, 2017: Spiraling pathways of global deep waters to the surface of the Southern Ocean. *Nat. Commun.*, **8**, 172, https://doi.org/10.1038/s41467-017-00197-0.

——, L. Talley, and M. Mazloff, 2019: A deep eastern boundary current carrying Indian Deep Water south of Australia. *J. Geophys. Res. Oceans*, **124**, 2218–2238, https://doi.org/10.1029/2018JC014569.

Thompson, A. F., and K. J. Richards, 2011: Low frequency variability of Southern Ocean jets. *J. Geophys. Res.*, **116**, C09022, https://doi.org/10.1029/2010JC006749.

Thompson, R. O., 1984: Observations of the Leeuwin current off Western Australia. *J. Phys. Oceanogr.*, **14**, 623–628, https://doi.org/10.1175/1520-0485(1984)014<0623:OOTLCO>2.0.CO;2.

Toole, J. M., and B. A. Warren, 1993: A hydrographic section across the subtropical South Indian Ocean. *Deep-Sea Res. I*, **40**, 1973–2019, https://doi.org/10.1016/0967-0637(93)90042-2.

Tsimplis, M., S. Bacon, and H. Bryden, 1998: The circulation of the subtropical South Pacific derived from hydrographic data. *J. Geophys. Res.*, **103**, 21 443–21 468, https://doi.org/10.1029/98JC01881.

Vallis, G. K., 2017: *Atmospheric and Oceanic Fluid Dynamics, Fundamentals and Large-Scale Circulation*. 2nd ed. Cambridge University Press, 946 pp.

Verdy, A., and M. Mazloff, 2017: A data assimilating model for estimating Southern Ocean biogeochemistry. *J. Geophys. Res. Oceans*, **122**, 6968–6988, https://doi.org/10.1002/2016JC012650.

von Storch, J.-S., C. Eden, I. Fast, H. Haak, D. Hernández-Deckers, E. Maier-Reimer, J. Marotzke, and D. Stammer, 2012: An estimate of the Lorenz energy cycle for the world ocean based on the STORM/NCEP simulation. *J. Phys. Oceanogr.*, **42**, 2185–2205, https://doi.org/10.1175/JPO-D-12-079.1.

Warren, B. A., 1973: Transpacific hydrographic sections at lats. 43°S and 28°S: The SCORPIO expedition—II. Deep water. *Deep-Sea Res. Oceanogr. Abstr.*, **20**, 9–38, https://doi.org/10.1016/0011-7471(73)90040-5.

——, and K. G. Speer, 1991: Deep circulation in the eastern South Atlantic Ocean. *Deep-Sea Res.*, **38A**, 281–322, https://doi.org/10.1016/S0198-0149(12)80014-8.

Well, R., W. Roether, and D. P. Stevens, 2003: An additional deep-water mass in Drake passage as revealed by ^{3}He data. *Deep-Sea Res. I*, **50**, 1079–1098, https://doi.org/10.1016/S0967-0637(03)00050-5.

Wijffels, S. E., J. M. Toole, and R. Davis, 2001: Revisiting the South Pacific subtropical circulation: A synthesis of world Ocean Circulation experiment observations along 32°S. *J. Geophys. Res.*, **106**, 19 481–19 513, https://doi.org/10.1029/1999JC000118.

Wolfe, C., and S. Bire, 2019: Eastern boundary currents an overturning in buoyancy-driven basins. *22nd Conf. on Atmospheric and Oceanic Fluid Dynamics*, Portland, ME, Amer. Meteor. Soc., 8.5, https://ams.confex.com/ams/22FLUID/meetingapp.cgi/Paper/360227.

Woodruff, S. D., R. J. Slutz, R. L. Jenne, and P. M. Steurer, 1987: A comprehensive ocean-atmosphere data set. *Bull. Amer. Meteor. Soc.*, **68**, 1239–1250, https://doi.org/10.1175/1520-0477(1987)068<1239:ACOADS>2.0.CO;2.

Wunsch, C., D. Hu, and B. Grant, 1983: Mass, heat, salt and nutrient fluxes in the South Pacific Ocean. *J. Phys. Oceanogr.*, **13**, 725–753, https://doi.org/10.1175/1520-0485(1983)013<0725:MHSANF>2.0.CO;2.

Yang, X., E. Tziperman, and K. Speer, 2020: Dynamics of deep ocean eastern boundary currents. *Geophys. Res. Lett.*, **47**, e2019GL085396, https://doi.org/10.1029/2019GL085396.